scientific reports

Check for updates

OPEN

Scalable synthesis of Cu–Sb–S phases from reactive melts of metal xanthates and effect of cationic manipulation on structural and optical properties

Tahani Alqahtani[1], Malik Dilshad Khan[2]✉, David J. Lewis[3]✉, Xiang Li Zhong[3] & Paul O'Brien[4,5]

We report a simple, economical and low temperature route for phase-pure synthesis of two distinct phases of Cu–Sb–S, chalcostibite ($CuSbS_2$) and tetrahedrite ($Cu_{12}Sb_4S_{13}$) nanostructures. Both compounds were prepared by the decomposition of a mixture of *bis*(*O*-ethylxanthato)copper(II) and *tris*(*O*-ethylxanthato)antimony(III), without the use of solvent or capping ligands. By tuning the molar ratio of copper and antimony xanthates, single-phases of either chalcostibite or tetrahedrite were obtained. The tetrahedrite phase exists in a cubic structure, where the Cu and Sb atoms are present in different coordination environments, and tuning of band gap energy was investigated by the incorporation of multivalent cationic dopants, i.e. by the formation of Zn-doped tetrahedrites $Cu_{12-x}Zn_xSb_4S_{13}$ (x = 0.25, 0.5, 0.75, 1, 1.2 and 1.5) and the Bi-doped tetrahedrites $Cu_{12}Sb_{4-x}Bi_xS_{13}$ (x = 0.08, 0.15, 0.25, 0.32, 0.4 and 0.5). Powder X-ray diffraction (p-XRD) confirms single-phase of cubic tetrahedrite structures for both of the doped series. The only exception was for $Cu_{12}Sb_{4-x}Bi_xS_{13}$ with x = 0.5, which showed a secondary phase, implying that this value is above the solubility limit of Bi in $Cu_{12}Sb_4S_{13}$ (12%). A linear increase in the lattice parameter *a* in both Zn- and Bi-doped tetrahedrite samples was observed with increasing dopant concentration. The estimated elemental compositions from EDX data are in line with the stoichiometric ratio expected for the compounds formed. The morphologies of samples were investigated using SEM and TEM, revealing the formation of smaller particle sizes upon incorporation of Zn. Incorporation of Zn or Bi into $Cu_{12}Sb_4S_{13}$ led to an increase in band gap energy. The estimated band gap energies of $Cu_{12-x}Zn_xSb_4S_{13}$ films ranges from 1.49 to 1.6 eV, while the band gaps of $Cu_{12}Sb_{4-x}Bi_xS_{13}$ films increases from 1.49 to 1.72 eV with increasing x.

Copper-based materials have attracted considerable attention due to their potential use as absorber materials for harvesting solar energy and as thermoelectric materials. Among such materials, copper indium gallium selenide (CIGS) has been considered as an excellent absorber material for solar cells with efficiency as high as 20.8%[1,2]. However, this material is associated with high cost and scarce elements (In and Ga). Cu_2ZnSnS_4 (CZTS) is a promising alternate earth abundant and low-toxic absorber material with a direct band gap and strong light absorption coefficient of over ~10^4 cm^{-1}[3,4]. Nevertheless, because of its complex phase diagram, obtaining CZTS as a single phase is a significant challenge[5].

Recently, ternary Cu–Sb–S systems have shown considerable potential as alternate absorber materials for inexpensive photovoltaic energy generation. These materials have close to optimal band gap energies for absorption of solar photonic flux combined with, high absorption coefficients and consist of modestly earth-abundant, and relatively non-toxic elements[6–9]. The Cu–Sb–S system exists in four crystallographic phases, i.e. chalcostibite ($CuSbS_2$), tetrahedrite ($C_{12}Sb_4S_{13}$), skinnerite (Cu_3SbS_3) and fematinite (Cu_3SbS_4). The band gap energies of

[1]School of Physics, Imam Abdulrahman Bin Faisal University, Dammam, Saudi Arabia. [2]Institute of Physical Chemistry, Polish Academy of Sciences, Kasprzaka 44/52, Warsaw 01-224, Poland. [3]Department of Materials, The University of Manchester, Oxford Road, Manchester M13 9PL, UK. [4]Department of Chemistry, The University of Manchester, Oxford Road, Manchester M13 9PL, UK. [5]Paul O'Brien is deceased. ✉email: malikdilshad@hotmail.com; david.lewis-4@manchester.ac.uk

these phases, vary between 1.1 and 1.8 eV and they show excellent absorption coefficients (i.e. over 10^5 cm^{-1}) with p-type electrical conductivity[6,9–15]. Among these four phases, chalcostibite $CuSbS_2$ (E_g ~ 1.4–1.5 eV)[9,11] and tetrahedrite $Cu_{12}Sb_4S_{13}$ (E_g ~ 1.2–1.7 eV)[13,16] have promising band gap values required for maximum solar energy utilization[6].

Chalcostibite $CuSbS_2$ has been regarded as a substitute material to $CuInS_2$ due to their analogous optical properties, with an added advantage of earth abundance of antimony and its lower cost compared to indium[17,18]. It has a direct band gap of 1.4–1.5 eV that is close to the optimum band gap range for solar energy conversion[19,20], large absorption coefficient of 10^4–10^5 cm^{-1} and suitable electrical properties for solar cell applications[7,21,22].

Another important phase of Cu–Sb–S, tetrahedrite $Cu_{12}Sb_4S_{13}$, has recently attracted attention, as it has emerged as a potential material for energy conversion applications. With its naturally low lattice thermal conductivity and its anisotropic crystal structure, $Cu_{12}Sb_4S_{13}$ is a candidate for thermoelectric energy generation via the Seebeck effect[23,24]. In addition, the strong absorption over a wide spectral range makes it useful as solar absorber material[8,25]. Naturally occurring tetrahedrite exists with varying compositions as $(Cu, Ag)_{10}(Cu, Zn, Fe, Cd, Hg)_2(Sb, Te, Bi, As)_4(S, Se)_{13}$ and can accommodate a range of substituents into the copper and antimony sites. The tetrahedrite has mixed Cu(I) and Cu(II) ions, which can be represented by $(Cu^+)_{10}(Cu^{2+})_2Sb_4S_{13}$[6]. The presence of metal cations with + 1, + 2 and + 3 oxidation states, provides flexibility with respect to incorporation of various isovalent dopants. However, in cubic tetrahedrite copper and antimony ions have different coordination environments, and therefore it is difficult to ascertain which cationic dopant will significantly influence the electronic properties of the tetrahedrite. Partial substitution (doping) of the copper, antimony and chalcogen sites $Cu_{12-x}A_xSb_{4-y}B_yS_{13-z}Se_z$ ($A = M^{2+}$; $B = M^{3+}$) by other elements is important to optimize the thermoelectric properties. These dopants could also lead to improved optical and magnetic properties. Pure (undoped) tetrahedrite $Cu_{12}Sb_4S_{13}$ is generally prepared by solid-state reactions, which require high temperatures and long melting and annealing procedures that takes as long as three weeks to ensure that products are phase pure[24,26,27]. Solution-phase and wet chemical approaches to develop faster and simpler methods of preparing phase-pure tetrahedrite have been reported to address this[6,15,16,28–33], and include hot injection[15], solvothermal[16,33], and spin coating or drop casting methodologies[31,34]. These approaches usually produce the tetrahedrite in the form of nanoscale particles and thin films, which show significantly different properties from those of bulk form. Rath and Haque et al.[34] deposited chalcostibite or tetrahedrite thin films using mixture of alkyl xanthate complexes of Cu and Sb, by varying the stoichiometric ratios of the precursors. The mixture solution was spin coated or drop casted on the substrates, which were annealed to obtain thin films. A layer thickness of 50–100 nm was achieved by spin coating and 1–2 μm by drop casting. Weller et al.[35] reported the solution-phase synthesis of tetrahedrite using a polyol process, which produced a nanostructured product (50–200 nm)[35]. It was shown that for these materials the thermopower was enhanced and thermal conductivity was decreased as compared to bulk tetrahedrite. Chen et al.[32] prepared spherical tetrahedrite nanocrystals with controllable size by the colloidal chemical route. The band gap energy was tuned from 2.45 to 1.82 eV by changing the particle size from 2 to 16 nm. However, the presence of capping agents or sulfonating agents in these solution-phase approaches can negatively affect the thermoelectric properties[36]. In addition, these solution-phase methods require expensive solvents for both synthesis and subsequent purification, which can significantly limit their large scale production[37].

This study reports a facile solvent-less method for the synthesis of orthorhombic chalcostibite and cubic tetrahedrite phases of copper antimony sulfide by using metal xanthate precursors. The absence of a solvent makes it environmentally friendly and economical as compared to hot injection and other colloidal routes[38]. The use of metal xanthates is beneficial as sulfur is already bonded to the metal atom in the precursor, which upon decomposition yields the metal sulfide, therefore eliminating the need of using an external sulfur source such as hydrogen sulfide. Likewise, the xanthate complexes are advantageous as they decompose at low temperatures (< 200 °C) and the by-products are volatile, which allows formation of clean and pure Cu–Sb–S materials at relatively low temperatures compared to solid state routes[39,40]. Such low temperatures are compatible with processing of these semiconductors onto polymeric substrates for flexible electronics.

We have demonstrate that two distinct phases of Cu–Sb–S, chalcostibite ($CuSbS_2$) and tetrahedrite ($Cu_{12}Sb_4S_{13}$), can be obtained by tuning the molar ratio of Cu to Sb xanthates in the direct pyrolysis of the powdered mixture. Furthermore, the band gap of tetrahedrite was tuned by doping of Zn and Bi using Zn and Bi xanthates respectively. We investigate the structural, morphological, compositional and optical properties of the systems.

Experimental

Chemicals. Potassium ethyl xanthogenate (96%), antimony(III) chloride ($SbCl_3$, ≥ 99.95%), copper(II) chloride dihydrate ($CuCl_2$ $2H_2O$, 99.99%), bismuth(III) chloride ($BiCl_3$, ≥ 98%), Zinc(II) nitrate hexahydrate ($Zn(NO_3)_2$ 6 H_2O, ≥ 98%), methanol (99.8%), ethanol (95.0%), chloroform ($CHCl_3$, ≥ 99%), Hexane (C_6H_{14}, ≥ 99%) were purchased from Sigma-Aldrich.

Materials Characterisation. The synthesized materials were characterized by similar techniques as used previously[41,42]. Briefly, elemental analysis and thermogravimetric analysis were performed in the micro-analytical laboratory of the University of Manchester. Mettler Toledo TGA/DSC1 star model was utilised to obtain the TGA data, at a temperature between 30 and 600 °C and a heating rate of 10 °C min^{-1} under N_2. X-Pert diffractometer was used to acquire p-XRD data, equipped with a Cu–K_α source (1.54059 Å). Each sample was scanned between 10° and 80° with 0.02° steps and 3 s per step, at 40 kV and 30 mA. Scanning electron microscopy (SEM) and energy-dispersive X-ray spectroscopy (EDX) measurements were obtained via a Philips XL30 FEG microscope, with an accelerating voltage of 10–20 kV. Raman spectra were recorded using a Renishaw 1000

Micro-Raman microscope with a 514 nm Argon ion laser. Transmission electron microscope (TEM) imaging and diffraction was performed using Tecnai F30 TEM operated at 300 kV.

Synthesis of antimony(III) ethylxanthate, $Sb[S_2COEt]_3$. The precursor was synthesized by using similar method as reported previously[41,42]. Briefly, potassium ethylxanthate (8.0 g, 49.9 mmol) was dissolved in ethanol (150 mL), followed by a gradual addition of antimony(III) chloride (3.79 g, 16.6 mmol) solution in ethanol (50 mL), with constant stirring for one hour at room temperature. The reaction mixture was filtered, product was washed with ethanol and DI water, dried under vacuum and recrystallised from chloroform to give bright yellow solid, yield: 7.1 g, 88%; m.p. 90.3 °C. Elemental analysis: calc. for $Sb[S_2COEt]_3$: C, 22.25%; H, 3.11%; S, 39.55%; Sb, 25.08%. Found: C, 22.61%; H, 3.07%; S, 39.71%; Sb, 24.15%. IR (cm^{-1}): 1220 ν(C–O); 1020 ν(C–S). ^{1}H-NMR ($CDCl_3$): δ 4.61 (q, J = 7.1 Hz, 2H, CH_2), δ 1.44 (t, J = 7.1 Hz, 3H, CH_3). ^{13}C NMR: δ 207.02 (S_2C), δ 72.07 (CH_2), δ 13.9 (CH_3).

Synthesis of copper(II) ethylxanthate, $Cu[S_2COEt]_2$. $Cu[S_2COEt]_2$ was prepared following the same method outlined above for $Sb[S_2COEt]_3$, however, copper(II) chloride dihydrate (4.25 g, 24.9 mmol) was used as the copper source, The resulting dark yellow solid was washed with distilled water and methanol and dried in vacuum. Yield 5.7 g, 75%; m.p. 170 °C. Elemental analysis: calc. for $Cu[S_2COEt]_2$: C, 23.3%; H, 3.3%; S, 41.3%; Cu, 20.5%. Found: C, 22.9%; H, 3.2%; S, 40.9%; Cu, 20.8%; IR (cm^{-1}): 1190 ν(C–O); 1007 ν(C–S).

Synthesis of bismuth(III) ethylxanthate, $Bi[S_2COEt]_3$. $Bi[S_2COEt]_3$ was prepared by following the method outlined above for $Sb[S_2COEt]_3$[41,42], however, bismuth(III) chloride (5.24 g, 16.6 mmol) was used as the bismuth source. The product was recrystallised from chloroform to give dark yellow solid. Yield 8.2 g, 86%; m.p. 110 °C. Elemental analysis: calc. for $Bi[S_2COEt]_3$: C, 18.86%; H, 2.64%; S, 33.53%; Bi, 36.49%. Found: C, 19.14%; H, 2.65%; S, 33.46%; Bi, 36.47%; IR (cm^{-1}): 1206 ν(C–O); 1018 ν(C–S). ^{1}H NMR ($CDCl_3$): δ 4.69 (q, J = 7.1 Hz, 2H, CH_2), δ 1.49 (t, J = 7.1 Hz, 3H, CH_3). ^{13}C NMR: δ 206.99 (S_2C), δ 71.3 (CH_2), δ 13.9 (CH_3).

Synthesis of Zinc(II) ethylxanthate, $Zn[S_2COEt]_2$. $Zn[S_2COEt]_2$ was prepared following the same method outlined above for $Sb[S_2COEt]_3$[41,42], however, zinc(II) nitrate hexahydrate (7.42 g, 24.9 mmol) was used as the zinc source. Recrystallization from chloroform resulted in white solid, yield 6.2 g, 80%; m.p. 120 °C. Elemental analysis: calc. for $Zn[S_2COEt]_2$: C, 23.4%; H, 3.3%; S, 41.7%; Zn, 21.3%. Found: C, 23.6%; H, 3.2%; S, 41.6%; Zn, 21.1%; IR (cm^{-1}): 1206 ν(C–O); 1022 ν(C–S). ^{1}H NMR ($CDCl_3$): δ 4.55 (q, J = 7.1 Hz, 2H, CH_2), δ 1.46 (t, J = 7.1 Hz, 3H, CH_3). ^{13}C NMR: δ 207.7 (S_2C), δ 77.2 (CH_2), δ 13.9 (CH_3).

Synthesis of Cu–Sb–S nanomaterials by melt thermolysis. Stoichiometric mixtures of copper xanthate ($Cu[S_2COEt]_2$) and antimony xanthate ($Sb[S_2COEt]_3$) were used to prepare Cu–Sb–S phases using melt method. In a typical procedure, different molar ratios of $Cu[S_2COEt]_2$ and $Sb[S_2COEt]_3$ complexes were grounded using a pestle and mortar for half an hour to ensure uniform mixing of the complexes. The homogenous mixture was then loaded evenly into a ceramic boat inside a reaction tube for heating. Subsequently, the reaction tube was heated in the furnace up to the chosen temperature (250 °C), under flow of nitrogen. After 1 h, the heating was turned off and the sample was allowed to cool to room temperature prior to collecting for characterisations.

Deposition of Cu–Sb–S thin films by doctor blade. Doctor blade technique is a simple, scalable and cost-effective way for the fabrication of uniform film on a variety of substrates. A blade is positioned over the substrate at an adjustable gap height from the substrate. A suitable amount of precursor solution (slurry) is placed in the front of the blade. The blade is then swiped linearly across the substrate, generating a uniform wet film layer[43,44]. The coating thickness is controlled by adjusting the gap between the blade and the substrate and the final wet layer should be roughly half of this gap from the substrate. However, many other factors can influence the thickness of the film including the precursor solution concentration, coating speed, surface tension of solution and the blade geometry[45,46]. In a typical procedure, mixture of Cu and Sb xanthate precursors was grounded using pestle and mortar for half an hour to ensure uniform mixing. Therefore, this is mixed with a few drops of hexane to produce a precursor slurry. The precursor slurry was dropped onto the glass substrate and swiped linearly by the doctor blade, followed by heating at 250 °C for one hour under nitrogen. The thickness of the dry film was found to be approximately 1.5 ± 0.1 μm as measured by SEM.

Result and discussion

In our melt synthesis of chalcostibite ($CuSbS_2$) and tetrahedrite ($Cu_{12}Sb_4S_{13}$), we have explored the use of the Cu xanthate ($Cu[S_2COEt]_2$) and Sb xanthate ($Sb[S_2COEt]_3$) as the Cu, Sb and S sources for the desired ternary sulfide material. The compositions of the obtained materials were adjusted by varying the molar ratio of the copper and antimony xanthate precursors. In addition, zinc xanthate ($Zn[S_2COEt]_2$) and bismuth xanthate ($Bi[S_2COEt]_3$) were also used for the preparation of the Zn and Bi doped tetrahedrite, respectively. Thermogravimetric analysis (TGA) (Supporting Information Fig. S1) shows that the decomposition from metal xanthates to the corresponding metal sulfides occur cleanly in one single step for all precursors at 150–200 °C. This indicates that the ternary copper antimony sulfide and quaternary Zn/Bi doped tetrahedrite materials can be obtained by the melt thermolysis of Cu, Sb, Zn or Bi xanthates at mild temperatures for a short period of time. Moreover, the by-products of the decomposition are volatile, allowing the clean formation of the materials without impurities.

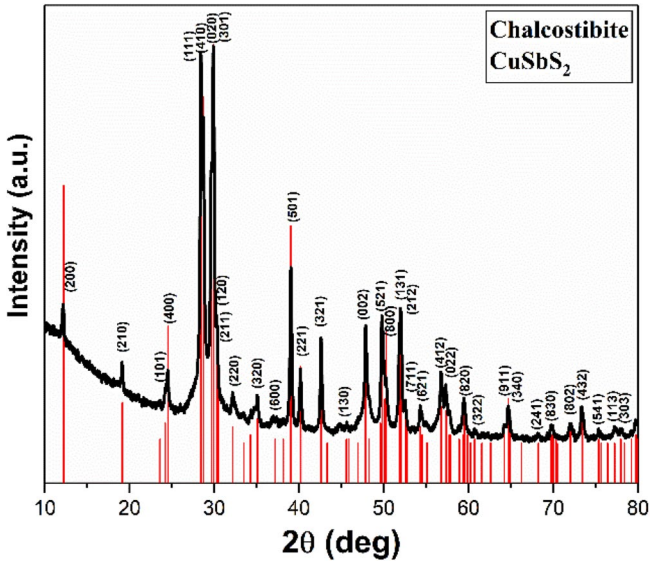

Figure 1. p-XRD pattern of chalcostibite $CuSbS_2$ nanomaterials prepared using 1: 1 molar ratio of Cu and Sb xanthates at 250 °C. Red lines show the positions of Bragg reflections from the standard reference pattern of orthorhombic $CuSbS_2$ (chalcostibite, ICDD: 01-088-0283).

Characterisation of Chalcostibite $CuSbS_2$ nanomaterials. The crystal structure and phase purity of the prepared cupper antimony sulfide nanomaterials are determined using powder-X-ray diffraction measurements (p-XRD). Figure 1 demonstrates the p-XRD patterns for the sample prepared using 1: 1 molar ratio of Cu and Sb xanthates at 250 °C. The position of the diffraction peaks in this powder pattern match well with a standard reference pattern for orthorhombic $CuSbS_2$ (chalcostibite, ICDD: 00-044-1417).

Scanning electron microscopy (SEM) in combintion with energy dispersive X-ray (EDX) spectroscopy were used to analyse the surface morphology, particle size and chemical composition of the prepared Cu–Sb–S nanomaterials. SEM images of a chalcostibite $CuSbS_2$ sample show spherical particles in nanometer-size range with an estimated average size of 89.8 ± 7.6, as presented in Fig. 2a,b. The small particle size is consistent with the Scherrer broadening observed in the p-XRD pattern presented earlier.

EDX spectra (Supporting Information Fig. S2a) display the characteristic emission lines of Cu, Sb and S. The chemical compositions of the chalcostibite $CuSbS_2$ sample was obtained and compared to the expected values (Table 1). The Cu: Sb: S ratios are approximate with the expected compositions, but having slightly Cu-rich stoichiometry. EDX elemental mapping was used to determine the spatial distribution of elements in the synthesized $CuSbS_2$ nanoparticles, as shown in Supporting Information Fig. S3a. The result reveals that the distribution of Cu, Sb and S elements is homogenous and uniform, with emission for all three elements co-localised in space as one may expect for such ternary phases.

Figure 3 shows the Raman spectrum (excitation wavelength of 514 nm) for the Chalcostibite $CuSbS_2$. We observe a peak in the spectrum at 331 cm^{-1} and a peak of lesser intensity at 250 cm^{-1}. Both peaks are associated with orthorhombic $CuSbS_2$ Chalcostibite; the peak at 331 cm^{-1} is attributed to the vibration of Sb–S bonds, whilst the peak at 250 cm^{-1} is assigned to the vibration of Cu–S bonds in reference spectra[47–49].

Characterisation of Tetrahedrite $Cu_{12}Sb_4S_{13}$ nanomaterials. Figure 4 presents the p-XRD patterns of tetrahedrite ($Cu_{12}Sb_4S_{13}$) nanomaterials obtained with different molar ratios of copper and antimony xanthate precursors. Initially, the tetrahedrite was prepared using 0.3 mmol of Cu-xanthate and 0.1 mmol of Sb-xanthate at 250 °C for 1 h (i.e. molar ratio = 3:1). However, this procedure yielded tetrahedrite with extra impurity peaks observed around 27.9° and 46.5° corresponding to $Cu_{2-x}S$ ICDD: 00-002-1292 (and marked by * in Fig. 4). Accordingly, the tetrahedrite nanomaterials with various Cu/Sb ratios which were synthesised at different temperatures and times were investigated to find out the optimal conditions for formation of pure-phase tetrahedrite. Varying annealing time and temperature, did not remove the impurity peaks associated with $Cu_{2-x}S$. However, we found that by decreasing the molar ratios of the copper/antimony xanthate precursors to 2.8:1, that the intensity of the reflections of the impurity peaks decreased. This effect was found to be monotonic upon further decrease in Cu:Sb molar ratio to 2.2:1, which further decreased the copper sulfide impurity. Ulitmately, by using 0.2 mmol of Cu-xanthate and 0.1 mmol of Sb-xanthate (i.e. molar ratio = 2:1) we found that we successfully produced a single phase corresponding to cubic tetrahedrite ($Cu_{12}Sb_4S_{13}$ ICDD: 01-088-0283) without presence of any other phases in the X-ray powder pattern, as illustrated in Fig. 4. Therefore, we concluded that using 2:1 molar ratio of Cu and Sb xanthate precursors is optimal in obtaining phase-pure tetrahedrite. Many studies have revealed that the presence of a small amount of impurity phases in the synthetic tetrahedrite cannot be avoided[50–59]. Previously, phase pure tetrahedrite nanoparticles have been prepared either by using capping agents, such as thiols, or incorporation of different dopants[52,60,61]. However, this study indicates that the solventless pyrolysis of the metal xanthate is advantageous in that it has demonstrated successful formation

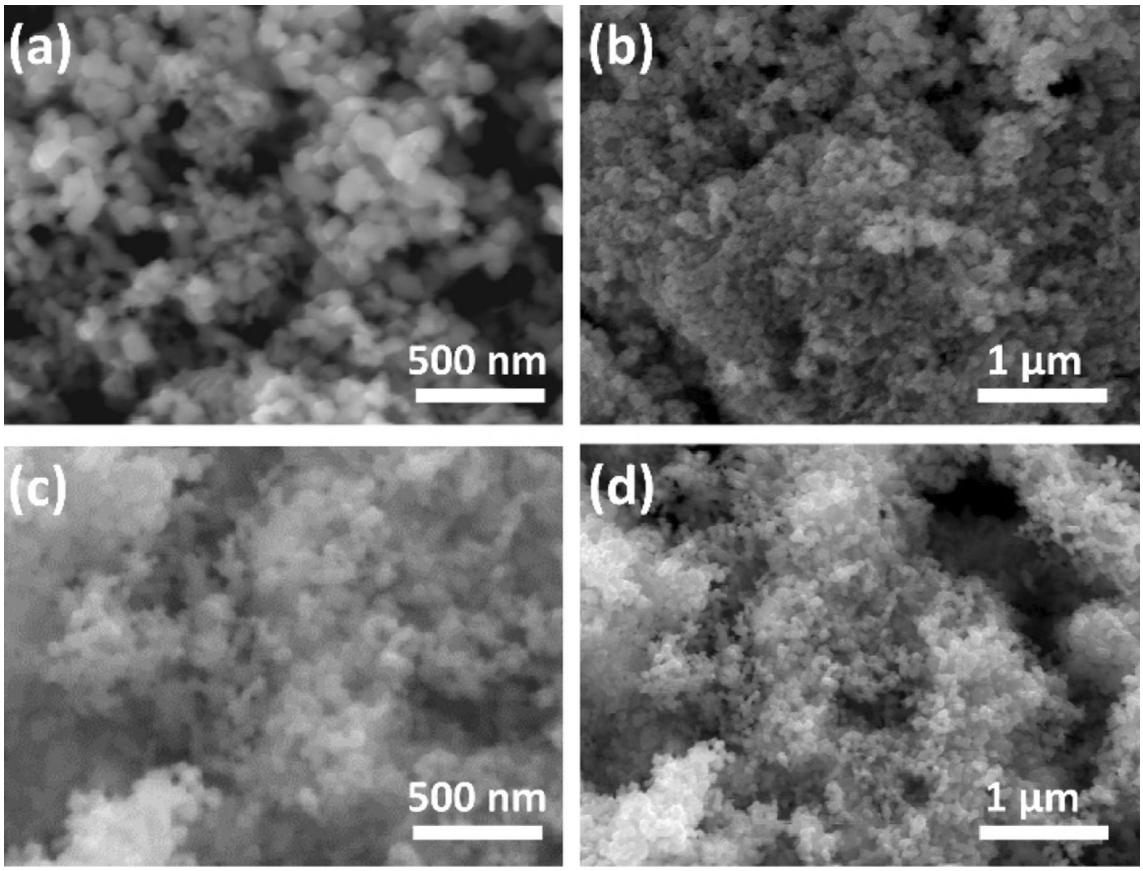

Figure 2. SEM images with different magnifications (**a**,**b**) for chalcostibite ($CuSbS_2$) and (**c**,**d**) for tetrahedrite ($Cu_{12}Sb_4S_{13}$).

Sample	Cu (at%)	Sb (at%)	S (at%)	Stoichiometry
$CuSbS_2$				
Expected	25	25	50	$CuSbS_2$
Sample	30.1	21.2	48.8	$Cu_{1.2}Sb_{0.85}S_{1.95}$
$Cu_{12}Sb_4S_{13}$				
Expected	41.4	13.8	44.8	$Cu_{12}Sb_4S_{13}$
3: 1 ratio	49.2	9.4	41.4	$Cu_{14.27}Sb_{2.73}S_{12}$
2: 1 ratio	41.1	14.2	44.6	$Cu_{11.92}Sb_{4.12}S_{12.93}$

Table 1. The content of Cu, Sb and S, in chalcostibite ($CuSbS_2$) and tetrahedrite ($Cu_{12}Sb_4S_{13}$) samples calculated from theoretical values and those found experimentally by EDX spectroscopy.

of the single-phase tetrahedrite $Cu_{12}Sb_4S_{13}$ of high purity in a short amount of time without the addition of any dopants or capping agents. The lattice parameter *a* of the $Cu_{12}Sb_4S_{13}$ was calculated from the p-XRD data and found to be 10.368 Å, which is consistent with previosuly reported literature values for cubic tetrahedrite (ICDD: 01-088-0283).

Figure 2c,d show SEM images at low and high magnifications of pure tetrahedrite $Cu_{12}Sb_4S_{13}$ prepared from 2:1 molar ratio of Cu and Sb xanthates. These images indicate the formation of pseudo-spherical particles at the nano-scale with an average size of 61 ± 8 nm. Similar morphologies for tetrahedrite nanoparticles (in the range of 50–200 nm) synthesised by modified polyol process have been reported[35]. The EDX spectra for tetrahedrite (Supporting Information Fig. S2b) displays the characteristic peaks of the three elements Cu, Sb and S, and the chemical compositions were obtained and compared to the expected values. For the tetrahedrite $Cu_{12}Sb_4S_{13}$, EDX spectroscopy was performed on samples synthesized using different molar ratios of Cu and Sb xanthates (Table 1). The expected values of tetrahedrite $Cu_{12}Sb_4S_{13}$ should have atomic % of Cu 41.4%, Sb 13.8% and S 44.8%. However, in the 3: 1 ratio we have obtained 49.2% of Cu, 9.4% of Sb and 41.4% of S, which is Cu-rich and Sb-deficient. In contrast, the final product of tetrahedrite using 2: 1 molar ratio of Cu and Sb is very close to the expected values for the pure tetrahedrite $Cu_{12}Sb_4S_{13}$ (41.1 of Cu, 14.2 of Sb and 44.6 of S), giving the formula

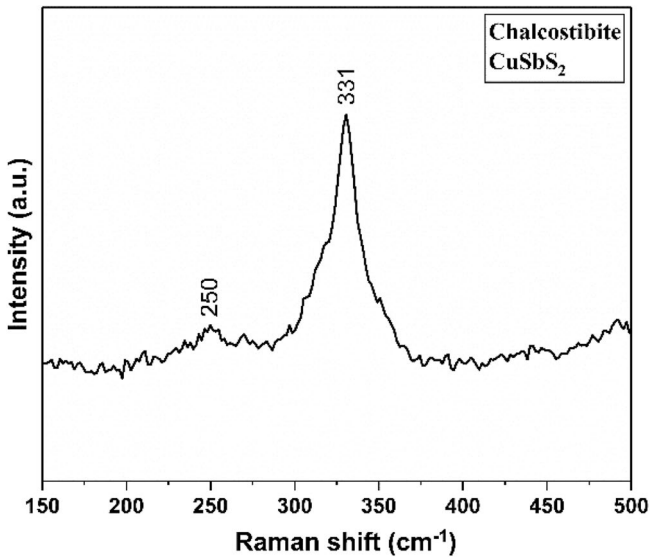

Figure 3. Raman spectrum of chalcostibite $CuSbS_2$ prepared using a 1: 1 ratio of Cu and Sb xanthate powders at 250 °C.

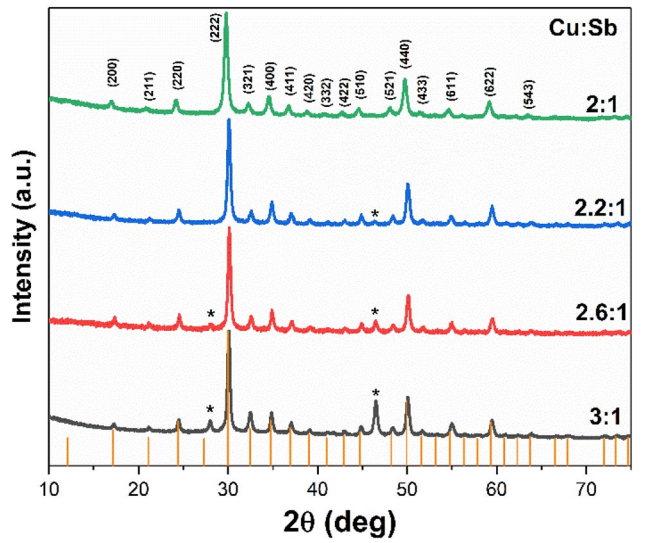

Figure 4. p-XRD patterns of tetrahedrite $Cu_{12}Sb_4S_{13}$ nanomaterials obtained at different molar ratios of copper and antimony xanthate precursors. Orange lines are from the standard reference pattern for cubic $Cu_{12}Sb_4S_{13}$ (tetrahedrite, ICDD: 01-088-0283). *Indicates the impurity peaks associated with formation of $Cu_{2-x}S$ (ICDD: 00-002-129).

of $Cu_{11.9}Sb_{4.1}S_{12.9}$. These results are consistent with the p-XRD results as the 3:1 ratio yielded an extra impurity phase, while using 2: 1 ratio exhibited a single tetrahedrite phase. Further inspection of TGA data for all complexes show that, beside antimony, the complexes decompose in a single step. The TGA of the antimony complex reveals that a major weight loss step occurs around 150 °C, and unlike other the complexes, undergoes another small weight loss step slightly below 250 °C. This may be attributed to an escape or volatilization of the residual product, which may slightly alter/decrease the amount of antimony content in tetrahedrite phase when 3:1 ratio is used, thereby resulting in copper rich product or introduction of impurity phase. Therefore a gradual decrease in the copper content result in the diminishing of the impurity phase and at 2:1 ratio, phase pure tetrahedrite was obtained. Both p-XRD and EDX spectroscopy revealed that the molar ratios of the Cu and Sb xanthate precursors plays an important role in the formation of single phase tetrahedrite $Cu_{12}Sb_4S_{13}$. EDX elemental mapping was performed to determine the elemental distribution of the synthesized $Cu_{12}Sb_4S_{13}$ nanoparticles, as shown in Supporting Information Fig. S3b. The result reveals that the distribution of Cu, Sb and S elements is homogenous and uniform. Furthermore, the decomposition of mixtures of Cu and Sb complexes in 3:1 and 2:1 ratio respectively, was also studied by TGA. It was observed that the complexes decompose completely at

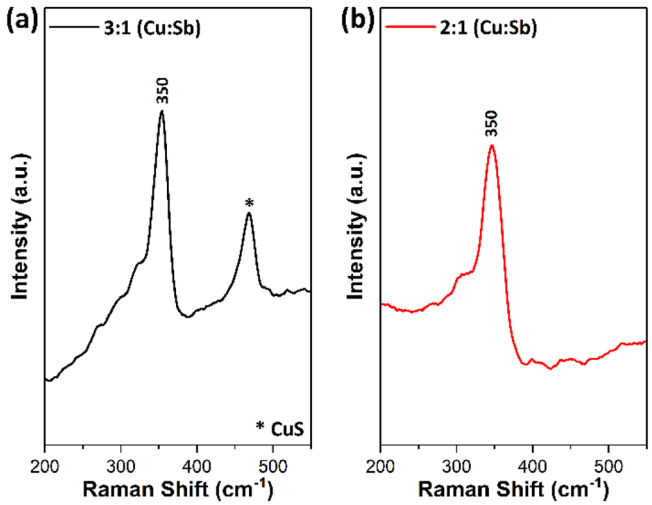

Figure 5. Raman spectra of tetrahedrite $Cu_{12}Sb_4S_{13}$ samples obtained at (**a**) 3:1 and (**b**) 2:1 molar ratio of Cu and Sb xanthate precursors.

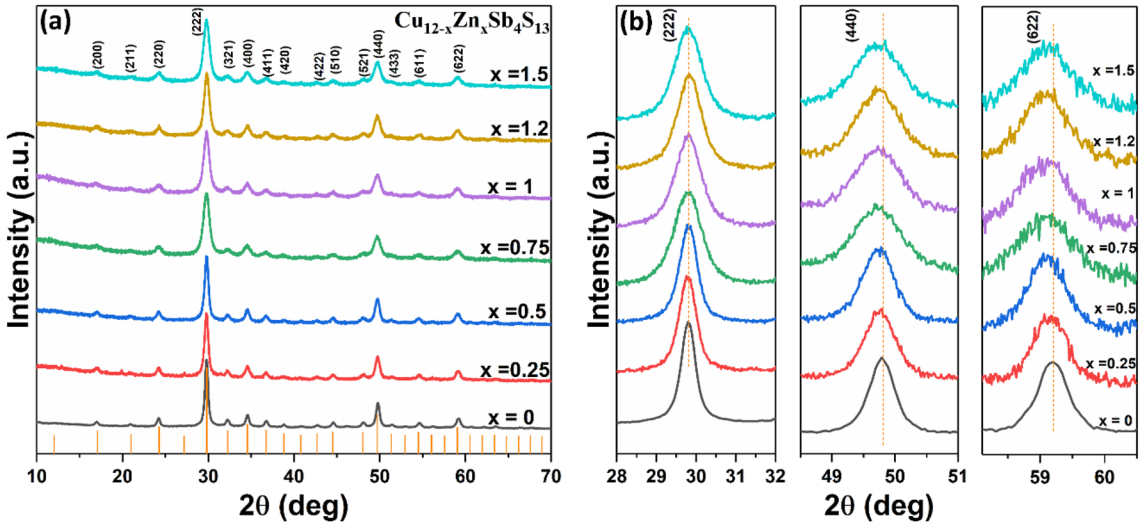

Figure 6. (**a**) p-XRD patterns of $Cu_{12-x}Zn_xSb_4S_{13}$ (x = 0.25, 0.5, 0.75, 1, 1.2, 1.5) and (**b**) the three main diffraction peaks (222), (440) and (622) of Zn-doped tetrahedrite samples. Orange lines are from standard ICDD: 01-088-0283 for cubic $Cu_{12}Sb_4S_{13}$ (tetrahedrite).

180 °C, resulting in the formation of tetrahedrite phase (Supporting Information Fig. S4). The tetrahedrite phase was stable up to 400 °C, after which a marginally small weight loss was observed between 400 and 500 °C. After 500 °C, a significant change was noticed which may show degradation of tetrahedrite phase via sulfur loss or other volatile by-products.

Transmission electron microscopy (TEM) and selected area electron diffraction (SAED) were performed and presented in Fig. 9. TEM images of the tetrahedrite $Cu_{12}Sb_4S_{13}$ nanoparticles show that the formation of agglomerated particles is in the nanometer range, with an estimated average size of 62 ± 9 nm, which is consistent with SEM results. Lattice fringes (Fig. 9b) were observed with estimated d-spacing of 2.99 Å, corresponding to the (222) lattice plane of cubic tetrahedrite $Cu_{12}Sb_4S_{13}$[6]. The inset of Fig. 9b shows the SAED pattern of the tetrahedrite $Cu_{12}Sb_4S_{13}$ nanomaterials, where circular rings were observed indicating the polycrystalline nature of the sample. There are six diffractions rings which correspond to the (220), (222), (400), (440), (611) and (622) lattice planes of the cubic tetrahedrite $Cu_{12}Sb_4S_{13}$[62], which is consistent with the p-XRD patterns of these materials (Fig. 4).

Raman spectra of tetrahedrite $Cu_{12}Sb_4S_{13}$ samples obtained for the materials produced with different molar ratios of Cu and Sb xanthate precursors are displayed in Fig. 5. Two Raman modes were observed for the sample obtained using 3:1 ratio (Cu: Sb). The Raman peak observed at 350 cm^{-1} is attributed to the cubic tetrahedrite $Cu_{12}Sb_4S_{13}$[63]. However, the Raman peak at 470 cm^{-1} corresponds to the binary $Cu_{2-x}S$ impurity phase[64,65]. For the 2: 1 ratio sample, only one vibrational mode was observed at 351 cm^{-1}, which can be assigned to the symmetric

x	Composition	Lattice parameters *a* (Å)	Elemental composition by EDX spectroscopy (atomic%)				Optical band gap energy, E_g (eV)
			Cu	Zn	Sb	S	
0	$Cu_{12}Sb_4S_{13}$	10.368	41.1	0	14.2	44.6	1.49
0.25	$Cu_{11.76}Zn_{0.24}Sb_4S_{13}$	10.369	39.2	0.7	14.5	45.6	1.50
0.5	$Cu_{11.52}Zn_{0.48}Sb_4S_{13}$	10.371	38.2	1.7	15.1	44.9	1.50
0.75	$Cu_{11.28}Zn_{0.72}Sb_4S_{13}$	10.373	38.1	2.2	15.5	44.1	1.51
1	$Cu_{11.04}Zn_{0.96}Sb_4S_{13}$	10.376	37.8	2.6	14.8	44.7	1.52
1.2	$Cu_{10.8}Zn_{1.2}Sb_4S_{13}$	10.377	37.0	3.0	15.4	44.6	1.54
1.5	$Cu_{10.56}Zn_{1.44}Sb_4S_{13}$	10.379	35.9	4.4	15.6	44.2	1.60

Table 2. Lattice parameter *a*, EDX compositional analysis and the estimated optical band gap (E_g) of $Cu_{12-x}Zn_xSb_4S_{13}$ (x = 0.25, 0.5, 0.75, 1, 1.2, 1.5).

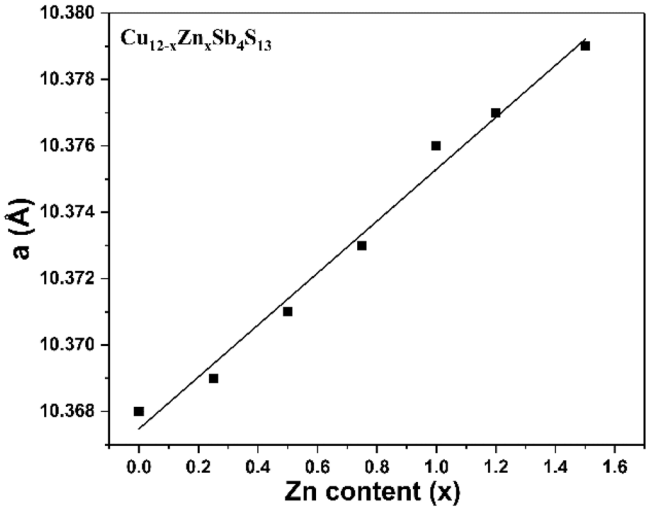

Figure 7. Lattice parameter *a* as a function of Zn stoichiometry (x) in $Cu_{12-x}Zn_xSb_4S_{13}$ (x = 0.25, 0.5, 0.75, 1, 1.2, 1.5).

stretching modes of the cubic tetrahedrite[66]. In this sample, no Raman peak is found for $Cu_{2-x}S$ (470 cm^{-1}) impurity phase. These results correlate well with the p-XRD analysis, where extra impurity peaks were observed only for the 3:1 ratio sample. Hence, the Raman study indicates that the 2:1 ratio of Cu and Sb xanthate is the optimal ratio to obtain phase pure tetrahedrite.

Characterisation of Zn^{2+} doped $Cu_{12}Sb_4S_{13}$ nanomaterials. Zn doped tetrahedrite nanomaterials were prepared by using the optimized quantities of Cu and Sb xanthate precursors (i.e. 2:1 ratio). p-XRD patterns (Fig. 6) reveal that the Zn-doped tetrahedrite $Cu_{12-x}Zn_xSb_4S_{13}$ (x = 0.25, 0.5, 0.75, 1, 1.2 and 1.5) nanocrystals have the same cubic crystal structure as the undoped tetrahedrite nanoparticles ($Cu_{12}Sb_4S_{13}$ ICDD: 01-088-0283). It has been widely reported that the substituted Zn atom replaces the Cu(1) site in CuS_4 tetrahedra within the tetrahedrite structure[60,67–70]. As can be seen from the p-XRD, the Zn is incorporated into the tetrahedrite, as there is no change in crystal structure and there is no evidence of the formation of a secondary zinc-rich phase e.g. ZnSs. Figure 6b displays the three main diffraction peaks of $Cu_{12-x}Zn_xSb_4S_{13}$ samples with various dopant levels, which are assigned to the (222), (440) and (622) Bragg planes of the tetrahedrite structure. The peaks were broadened as the Zn dopant level increased in the samples; this broadening effect is likely brought about by the changes in size of the nanocrystals, which we discuss later. Furthermore, the maximum intensity of the diffraction peak (222) showed no shift upon increasing the Zn doping content. However, the other two diffraction peaks, namely the (444) and (622) planes, displayed a small shift towards lower angle as the Zn dopant concentration increased in the samples. The shift of the diffraction peaks indicates an expansion in the lattice cell due to the atomic radius of Zn^{2+} (0.68 Å) which is slightly larger than that of Cu^{1+} (0.60 Å)[71]. Table 2 shows the unit cell lattice parameters *a* for $Cu_{12-x}Zn_xSb_4S_{13}$ samples, which were calculated from the X-ray-diffraction data using the lattice relation for cubic structure; $d = \frac{a}{\sqrt{h^2+k^2+l^2}}$, where d is lattice plane spacing and (hkl) are the Miller indices of the plane[72]. The calculated lattice parameter *a* of all samples is plotted as a function of Zn composition, as illustrated in Fig. 7. The lattice parameter *a* was found to increase from 10.368 to 10.379 Å when increasing the Zn content in the samples from x = 0 to x = 1.5. Similar behaviour was observed in the Zn-doped

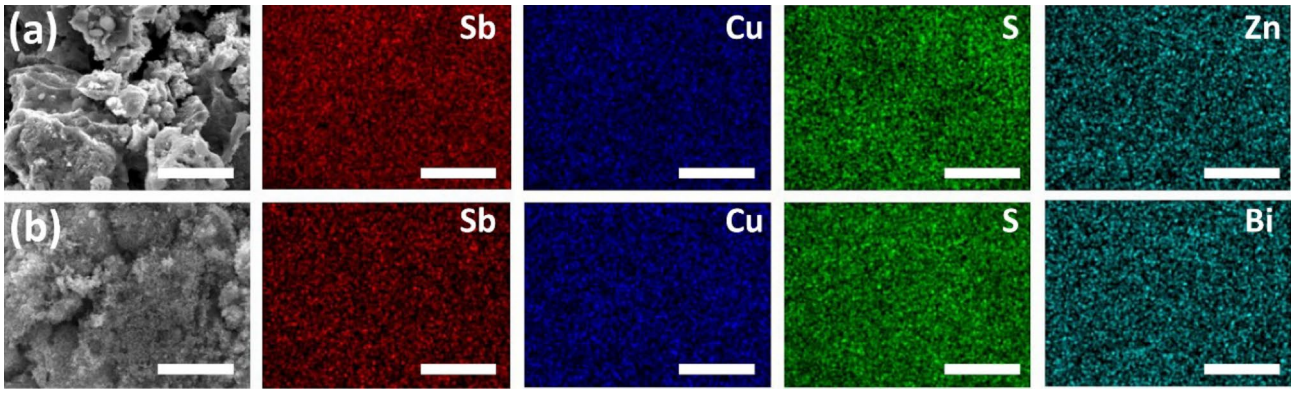

Figure 8. EDX elemental mapping (20 kV) of Cu Kα, Sb Lα, S Kα and Zn Kα/Bi Mα for (**a**) $Cu_{12-x}Zn_xSb_4S_{13}$ (x = 1.5) and (**b**) $Cu_{12}Sb_{4-x}Bi_xS_{13}$ (x = 0.5). Scale bars = 5 µm.

tetrahedrite series by May et al.[73] where the lattice parameter increases from 10.3221 Å for pure tetrahedrite to 10.3805 Å for $Cu_{10}Zn_2Sb_4S_{13}$.

SEM images that show the morphologies of the Zn-doped tetrahedrite $Cu_{12-x}Zn_xSb_4S_{13}$ samples with different Zn contents are illustrated in Fig. S5 (Supporting Information). The SEM images reveal particles in the nano-size range with spherical to irregular shapes. Furthermore, the incorporation of the Zn into the tetrahedrites reduces the particle size from 61 ± 8 for pure tetrahedrite to 28 ± 3 nm for 12% Zn-doped tetrahedrite. This finding correlates well with p-XRD data collected for these samples as the peaks broaden with increasing Zn in the samples. A similar observation was reported by Battiston et al.[74], who identified that adding Zn yielded a smaller particle size. EDX spectrscopy of the $Cu_{12-x}Zn_xSb_4S_{13}$ (x = 0.25, 0.5, 0.75, 1, 1.2 and 1.5) samples confirm the presence of copper, antimony, sulphur and zinc elements in all products obtained at different x (Supporting Information Fig. S6). Table 2 summarizes the EDX results of the Zn series samples. In all the samples, the observed compositions in the Zn-doped-tetrahedrite is close to the expected one, having slightly Sb-rich composition in all samples. Moreover, the compositions of all samples measured by EDX confirm that the substituted Zn atom replaces the Cu sites in the tetrahedrite structure. Figure 8a demonstrates the elemental mapping of the sample at the highest content of Zn (x = 1.5) for Cu Kα, Sb Lα, S Kα and Zn Kα at 20 kV. This indicates a homogeneous spatial distribution of the elements.

TEM and SAED were used in tandem to examine the crystalline structure of the nanoscale Zn-doped tetrahedrite $Cu_{12-x}Zn_xSb_4S_{13}$. TEM imaging of $Cu_{12-x}Zn_xSb_4S_{13}$ with x = 1.5 (Fig. 9c) reveals that with incorporation the Zn into the tetrahedrite, smaller particles were obtained, with an estimated average size of 28 ± 4 nm, which is consistent with the SEM data[60]. The *d*-spacing from lattice fringes was measured to be 3.01 Å (Fig. 9d), which corresponds to the (222) plane of cubic tetrahedrite, which is slightly larger compared to the *d*-spacing for pure tetrahedrite (2.99 Å). This obtained *d*-spacing implies that, besides slight lattice expansion, no phase change occurred on incorporation of 12 at% Zn into the tetrahedrite structure. The inset of Fig. 9d shows the SAED pattern of the $Cu_{12-x}Zn_xSb_4S_{13}$ with x = 1.5 sample. The pattern confirms that the Zn-doped nanomaterials are polycrystalline with the rings indexed to the cubic structure of tetrahedrite, which matches the XRD peaks shown in Fig. 6.

Raman spectra of Zn-tetrahedrite $Cu_{12-x}Zn_xSb_4S_{13}$ (x = 0.25, 0.5, 0.75, 1, 1.2 and 1.5) samples (Fig. 10) showed a single peak at 350 cm^{-1}, which is the characteristic peak of the cubic tetrahedrite phase[63]. Upon increasing the amount of Zn in the tetrahedrite, the Raman peak shifts slightly to higher frequencies from 350 to 355 cm^{-1}. This shift in the Raman peak potentially attributed to the change in the lattice vibrations after incorporation of Zn into the tetrahedrite structure. These results are in agreement with a previous study by Bera et al.[75], which established that the Raman peak position of the Zn-substituted tetrahedrite ($Cu_{10}Zn_2Sb_4S_{13}$) nanocrystals moves to a higher frequency in the Raman spectra compared to the pure tetrahedrite ($Cu_{12}Sb_4S_{13}$)[75]. Bera and others[75,76] attribute the shift of these Raman peaks is attributed to the changes in metal—sulfur bond force constants, f_{m-s}. The Cu–S bonds are partly replaced by Zn–S during the formation of the Zn-doped tetrahedrite. As a result, a shift to higher frequencies was observed in the Raman spectra because of the $f_{Zn-S} > f_{Cu-S}$, which attributed to the higher mass of zinc in comparison with copper[75,76].

Bi^{3+} doped $Cu_{12}Sb_4S_{13}$ nanomaterials. Bi doped tetrahedrite nanomaterials were prepared by using the optimized quantities of Cu and Sb xanthate precursors (i.e. 2:1 ratio). p-XRD shows that $Cu_{12}Sb_{4-x}Bi_xS_{13}$ (x = 0.08, 0.15, 0.25, 0.32, 0.4 and 0.5) nanomaterials also exhibit the cubic tetrahedrite structure ($Cu_{12}Sb_4S_{13}$ ICDD: 01-088-0283) with, in the main, no secondary phases observed (Fig. 11a). Only the sample at the Bi content of x = 0.5 (12%) shows two minor additional peaks corresponding to Bi_2S_3 (as indicated by asterisks), implying that this value is above the solubility limit of Bi in $Cu_{12}Sb_4S_{13}$. As the Bi content increases in the samples, the most intense diffraction peak, which corresponds to the (222) plane is gradually shifted towards lower angles, as can be seen in Fig. 11b. In addition, the other two peaks indexed to the (440) and (662) planes exhibit a shift towards lower angle as the Bi dopant concentration increased in the samples (Supporting Information Fig. S7). This shift indicates an expansion in the crystal structure. The lattice parameters *a* of $Cu_{12}Sb_{4-x}Bi_xS_{13}$

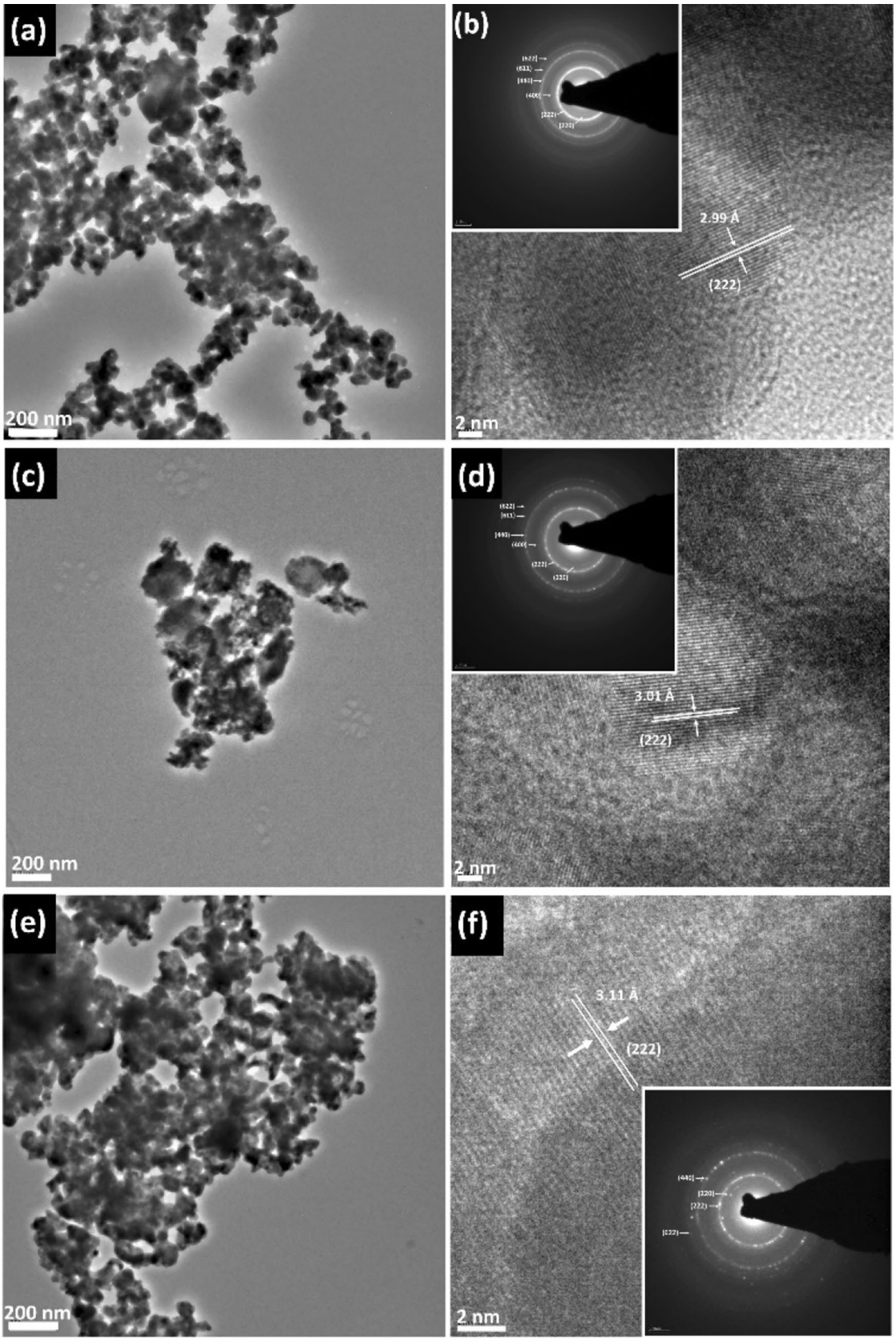

Figure 9. (**a**) TEM image of $Cu_{12}Sb_4S_{13}$ and (**b**) TEM micrograph showing lattice spacings of 2.99 Å for $Cu_{12}Sb_4S_{13}$, was assigned to the (222) plane of the cubic tetrahedrite. Inset in (**b**) shows the corresponding SAED pattern. (**c**) TEM image of $Cu_{12-x}Zn_xSb_4S_{13}$ for x = 1.5 and (**d**) TEM micrograph showing lattice spacings of 3.01 Å for $Cu_{12-x}Zn_xSb_4S_{13}$, x = 1.5, was assigned to the (222) plane of the cubic tetrahedrite. Inset in (**d**) shows the corresponding SAED pattern. (**e**) TEM image of $Cu_{12}Sb_{4-x}Bi_xS_{13}$ for x = 0.5 and (**f**) TEM micrograph showing lattice spacings of 3.11 Å for $Cu_{12}Sb_{4-x}Bi_xS_{13}$, x = 0.5, was assigned to the (222) plane of cubic tetrahedrite. Inset in (**f**) shows the corresponding SAED pattern.

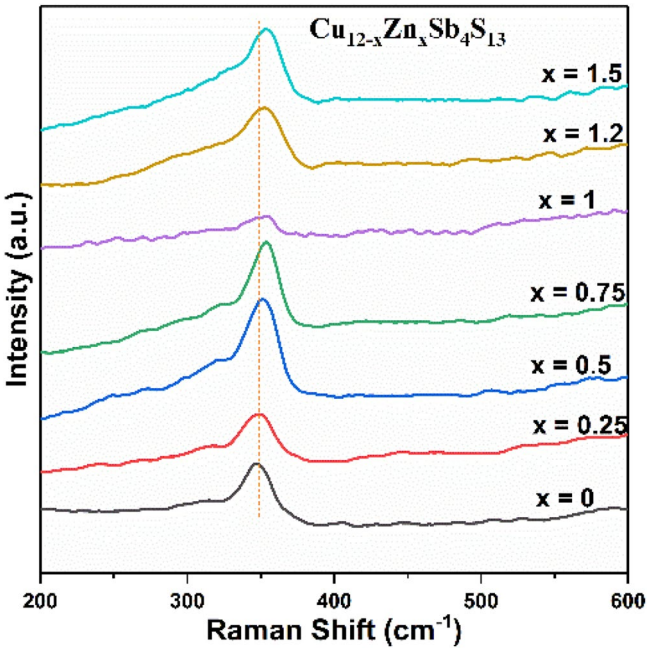

Figure 10. Raman spectra of Zn-doped tetrahedrite $Cu_{12-x}Zn_xSb_4S_{13}$ (x = 0.25, 0.5, 0.75, 1, 1.2, 1.5).

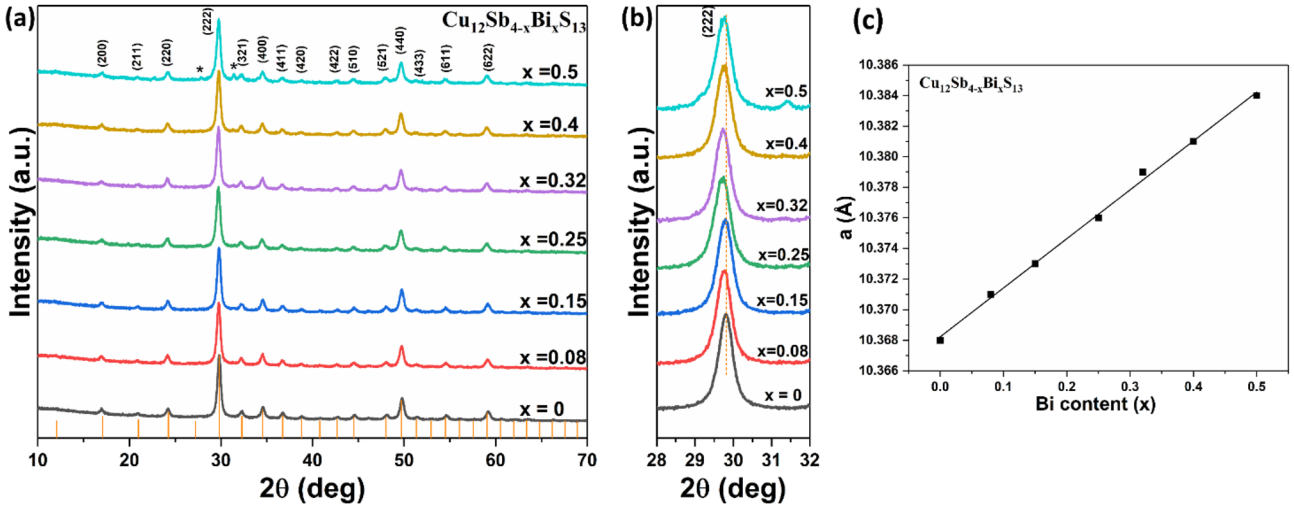

Figure 11. (**a**) p-XRD patterns of $Cu_{12}Sb_{4-x}Bi_xS_{13}$ (x = 0.08, 0.15, 0.25, 0.32, 0.4 and 0.5) and (**b**) the maximum intensity peak (222) of Bi-doped tetrahedrite samples. Orange lines are from standard ICDD: 01-088-0283 for cubic $Cu_{12}Sb_4S_{13}$ (tetrahedrite). (**c**) Lattice parameter a as a function of Bi composition.

X	Composition	Lattice parameters a (Å)	Elemental composition by EDX (atomic%)				E_g (eV)
			Cu	Sb	Bi	S	
0	$Cu_{12}Sb_4S_{13}$	10.368	41.1	14.2	0	44.6	1.49
0.08	$Cu_{12}Sb_{3.92}Bi_{0.08}S_{13}$	10.371	40.8	14.3	0.5	44.4	1.53
0.15	$Cu_{12}Sb_{3.84}Bi_{0.16}S_{13}$	10.373	40.4	13.8	0.8	45.0	1.56
0.25	$Cu_{12}Sb_{3.76}Bi_{0.24}S_{13}$	10.376	40.7	14.6	0.9	43.8	1.58
0.32	$Cu_{12}Sb_{3.68}Bi_{0.32}S_{13}$	10.379	40.5	13.9	1.2	44.4	1.59
0.4	$Cu_{12}Sb_{3.6}Bi_{0.4}S_{13}$	10.381	40.9	14.2	1.5	43.4	1.66
0.5	$Cu_{12}Sb_{3.52}Bi_{0.48}S_{13}$	10.384	40.6	13.8	1.8	43.8	1.72

Table 3. Lattice parameters a, EDX compositional analysis and the estimated band gap (E_g) of $Cu_{12}Sb_{4-x}Bi_xS_{13}$ (x = 0.08, 0.15, 0.25, 0.32, 0.4 and 0.5).

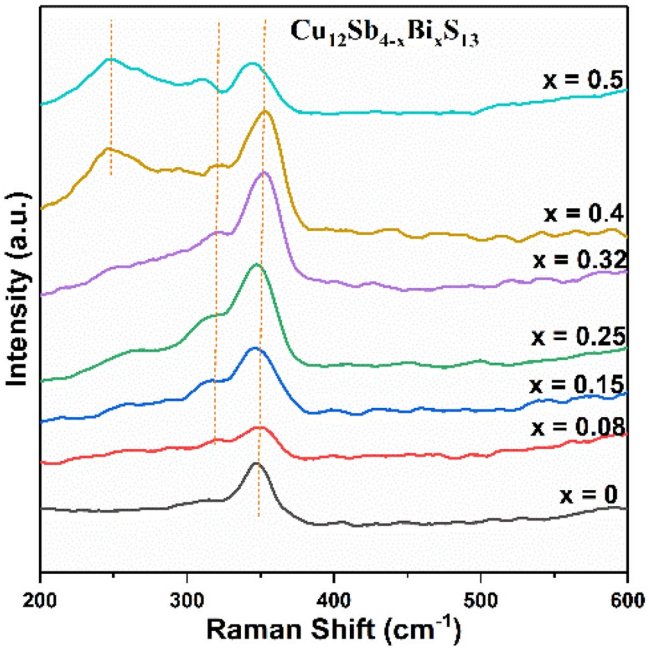

Figure 12. Raman spectra of Bi-doped tetrahedrite $Cu_{12}Sb_{4-x}Bi_xS_{13}$ (x = 0.08, 0.15, 0.25, 0.32, 0.4 and 0.5).

samples with various doping contents were calculated from the X-ray-diffraction data (Table 3) and were found to increase linearly with increasing the Bi content in the samples, as shown in Fig. 11c. This increase in the lattice parameter confirms the substitution of Bi at Sb sites, since ionic radii for Bi^{3+} (0.96 Å) is slightly larger than that for Sb^{3+} (0.76 Å)[71]. Similar behaviour was reported by Kumar et al.[77] for the Bi-doped samples. In this instance the lattice parameter *a* increases from 10.326 Å for undoped tetrahedrite to 10.375 Å for Bi-doped tetrahedrite $Cu_{12}Sb_{4-x}Bi_xS_{13}$ with x = 0.8. The changes in the lattice parameter values for the Bi-doped samples are larger than that of the Zn-doped samples. This is a result of the radius difference between Bi (0.96 Å) and Sb (0.76 Å) which is larger than that between Cu (0.6 Å) and Zn (0.68 Å) (see Supporting Information Fig. S8). This observation is consistent with the previous study by Kumar et al.[55]. They compared the lattice parameters for various dopants at Cu site i.e. $Cu_{12-x}M_xSb_4S_{13}$, (where M = Ni, Cd, Co, Zn, Mn) at x = 1.5. They found that as the ionic radii of these doping elements increased (Ni < Co < Zn < Mn < Cd), expansion in the crystal structure takes place, causing an increase in the lattice parameters (follow the trend Ni < Co < Zn < Mn < Cd)[55].

The SEM images of the Bi-doped tetrahedrite $Cu_{12}Sb_{4-x}Bi_xS_{13}$ samples with different Bi content are illustrated in Fig. S9 (Supporting Information). The morphologies of all the Bi doped samples is similar to that of the pure tetrahedrite. Limited differences were observed as the Bi content increased in the sample. The particle size of the sample at the highest content of Bi (x = 0.5) was found to be in the range of 62 ± 9, which is very similar to that of the undoped tetrahedrite (61.2 ± 8). The EDX spectra of the $Cu_{12}Sb_{4-x}Bi_xS_{13}$ indicated the characteristic peaks of copper, antimony, sulphur and bismuth in all samples obtained at different x and no impurities were observed (Supporting Information Fig. S6). Table 3 summarizes the EDX results of the Bi series samples. In all the samples, the observed compositions in the Bi-doped-tetrahedrite is close to the expected values. Figure 8b shows EDX elemental mapping of the sample at the highest content of Bi (x = 0.5) for the Cu Kα, Sb Lα, S Kα and Bi Mα emissions, which indicate a homogeneous distribution of the elements at the scale investigated.

The structure of the $Cu_{12}Sb_{4-x}Bi_xS_{13}$ with x = 0.5 sample was further investigated by using TEM and SAED. The images collected are displayed in Fig. 9e,f. The TEM image of this sample shows similar particle sizes to that of pure tetrahedrite, with an estimated average size of 62 ± 7 nm. This is consistent with the SEM data discussed previously (Fig. 9e). The d-spacing for the (222) plane of the $Cu_{12}Sb_{4-x}Bi_xS_{13}$ for x = 0.5 was 0.311 nm (Fig. 9f) which is larger than that for pure tetrahedrite (0.302 nm) due to bismuth incorporation. This increase in the *d*-spacing may be caused by both the higher mass of Bi and the longer Bi–S distances compared with Sb[78]. The SAED pattern of the $Cu_{12}Sb_{4-x}Bi_xS_{13}$ with x = 0.5 nanomaterial (inset of Fig. 9f) displays clear ordered diffraction rings, corresponding to the (220), (222), (440) and (622) lattice planes of the cubic tetrahedrite, which agree well with the XRD pattern in Fig. 11.

The Raman spectra for all the Bi-doped tetrahedrite $Cu_{12}Sb_{4-x}Bi_xS_{13}$ (x = 0.08, 0.15, 0.25, 0.32, 0.4 and 0.5) samples are shown in Fig. 12. A broad band is observed at approximately at 351 cm^{-1} for all the samples, which is the characteristic peak of the cubic tetrahedrite phase[63]. Also, a peak begins to emerge at 319 cm^{-1} for the x = 0.08 sample, which assigned to the symmetric bending mode of the cubic tetrahedrite. This new peak shifts towards lower frequencies as the Bi content is increased. The absence of this peak in the pure tetrahedrite sample might be attributed to the poor crystallinity of the sample or the peak was too weak to be identified[28]. In addition, another peak begins to appear at 250 cm^{-1} when the Bi content increased to x = 0.4, which corresponds to the B_{1g} anti-symmetric stretching mode for orthorhombic Bi_2S_3[40,79]. However, in the XRD data, the presence of Bi_2S_3 peaks is found only at the Bi content of x = 0.5 (12%) sample which highlights the importance of a multiple

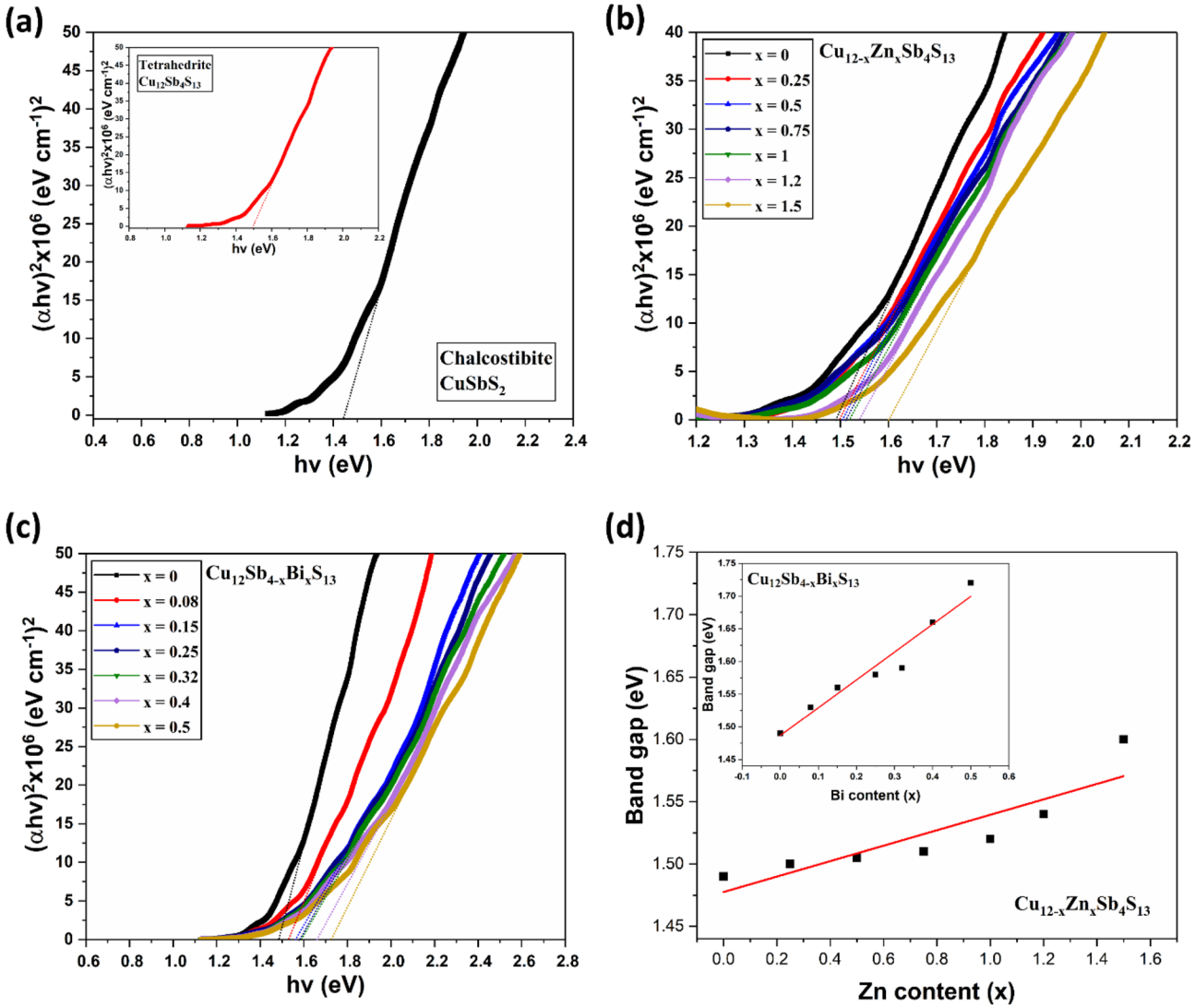

Figure 13. Estimation of optical band gap in Cu-Sb-S materials. Tauc plots for the (**a**) $CuSbS_2$ and $Cu_{12}Sb_4S_{13}$ (inset), (**b**) $Cu_{12-x}Zn_xSb_4S_{13}$ (x = 0.25, 0.5, 0.75, 1, 1.2, 1.5) and (**c**) $Cu_{12}Sb_{4-x}Bi_xS_{13}$ (x = 0.08, 0.15, 0.25, 0.32, 0.4 and 0.5). (**d**) Variation of the band gap for $Cu_{12-x}Zn_xSb_4S_{13}$ samples as a function x_{Zn}, and the inset shows the variation of the band gap for $Cu_{12}Sb_{4-x}Bi_xS_{13}$ samples as a function x_{Bi}.

technique approach to characterisation for these materials. The shift of the peaks towards lower wavenumbers were detected as the amount of Bi increased in the samples. This may be attributed to the higher mass of Bi and the longer Bi–S distance in contrast with Sb[79,80].

Optical band gap. For optical bandgap measurements, thin-film samples of chalcostibite, tetrahedrite and Zn/Bi-doped tetrahedrite were prepared by doctor bladed using a slurry of Cu, Sb, Zn or Bi xanthates in hexane and deposited on a glass substrate. The deposited precursors were heat treated in a quartz tube under a flow of nitrogen at 250 °C for 1 hour. The films were characterized by p-XRD and EDX spectroscopy to confirm the formation of desired phases and the diffraction patterns indicated that the deposited films have exact same phase as obtained from the powdered products (Supporting Information Fig. S10). The elemental composition of the films was determined by EDX spectroscopy and the stoichiometry of the films was comparable to the powdered films (Supporting Information Table S1–S3). The surface analysis of the films indicated that the deposited films were not of good quality and were full of cracks (Supporting Information Fig. S11, S12). The adherence to the glass substrate was not strong, and the particulate material can be easily scratched off from the substrate. The probable reasons for low quality of the films may be high volatility of hexane, leaving the slurry dried on the substrate and the escape of volatile gases (COH and ethene) during the thermal decomposition of the xanthate complexes, may have resulted in the formation of cracked surface and loosely bound films.

Optical absorption spectra of these samples were recorded in the wavelength range of 400–1100 nm (Supporting Information Fig. S13a,b). The band gap of the films can be calculated using the formula $(\alpha h\nu)^n = A(h\nu - Eg)$: Eg is the optical band gap, $h\nu$ is the photon energy, α is the absorption coefficient, A is a constant characteristic of the material, and n = 2, ½ for allowed direct and allowed indirect transitions, respectively. Chacostibite $CuSbS_2$

and tetrahedrite $Cu_{12}Sb_4S_{13}$ ternary phases are reported as direct band gap materials[30,81]. (Note: Some reports have also indicated the presence of both direct and indirect band gaps for $CuSbS_2$ phase[6], and the probable reason is that $CuSbS_2$ exists in layered structure and it has been shown that the band gap of layered semiconducting materials can be changed from indirect to direct by tuning the thickness of the nanosheets[82]) Furthermore, plots of the $(\alpha h\nu)^n$ versus hν for n = 2 and ½ show a linear behaviour for n = 2, which confirm the presence of a direct transition in both phases. Figure 13a–c present the estimation of band gaps using the Tauc plots for all Cu–Sb–S samples. For the chacostibite nanomaterials, the direct band gaps were estimated to be 1.44 eV; very close to the reported values for this material[9,47,83]. The value of the band gap for the pure tetrahedrite was estimated to be 1.49 eV, which was also close to the reported value[15,31]. For the $Cu_{12-x}Zn_xSb_4S_{13}$, the band gaps are estimated to be ~ 1.49, 1.5, 1.505, 1.51, 1.52, 1.54, and 1.6 eV, respectively, as the Zn content increased in the films from x = 0 to x = 1.5. A similar observation has been reported by Bera et al.[75], as they found the energy band gap of the Zn-substituted tetrahedrite ($Cu_{10}Zn_2Sb_4S_{13}$) nanocrystals increased compared to the pure tetrahedrite ($Cu_{12}Sb_4S_{13}$) nanocrystals. Similarly, the band gaps of $Cu_{12}Sb_{4-x}Bi_xS_{13}$ samples are estimated to be ~1.49, 1.53, 1.56, 1.58, 1.59, 1.66, and 1.72 eV, respectively, with increasing Bi content in the films from x = 0 to x = 0.5. Figure 13d shows the variation of the band gap of the Zn and Bi-doped samples as a function of x, demonstrating that the band gap of both doped samples increases with increasing dopant concentration. The increase of the band gap with increasing dopant into the tetrahedrite was significant in Bi doped samples compared to Zn-doped samples (see Supporting Information Fig. S14).

Conclusions

Toward the synthesis of chalcostibite ($CuSbS_2$) and tetrahedrite ($Cu_{12}Sb_4S_{13}$), the use of the Cu (II) xanthate ($Cu[S_2COEt]_2$) and Sb (III) xanthate ($Sb[S_2COEt]_3$) has been explored as the Cu, Sb and S sources for the desired ternary copper antimony sulfide nanomaterials. The compositions of the obtained materials were adjusted by varying the molar ratio of the copper and antimony xanthate precursors. Powder XRD and Raman spectroscopy indicates that using the expected ratios of Cu and Sb precursors for the pure tetrahedrite synthesis (3:1 ratio) yielded an extra binary copper sulfide impurity phase, while using less amount of Cu precursor (2:1 ratio) produced a single-phase tetrahedrite without the presence of any impurities. Zn-doped tetrahedrites $Cu_{12-x}Zn_xSb_4S_{13}$ (x = 0.25, 0.5, 0.75, 1, 1.2 and 1.5) and Bi-doped tetrahedrites $Cu_{12}Sb_{4-x}Bi_xS_{13}$ (x = 0.08, 0.15, 0.25, 0.32, 0.4 and 0.5) were also synthesized using Zn(II) xanthate ($Zn[S_2COEt]_2$) and Bi(III) xanthate ($Bi[S_2COEt]_3$) as the Zn and Bi sources. P-XRD analysis confirm the presence of cubic tetrahedrite for all two doped series. The only exception was for $Cu_{12}Sb_{4-x}Bi_xS_{13}$ with x = 0.5, which showed a secondary phase, implying that this value is above the solubility limit of Bi in $Cu_{12}Sb_4S_{13}$ (12%). We found that the lattice parameters *a* in both tetrahedrite samples with Zn- and Bi-doping increased with increasing dopant concentration. SEM images indicated the formation of smaller particle sizes with Zn incorporation into the tetrahedrite, whereas Bi doped samples exhibited a similar particle size to that of pure tetrahedrite. The estimated band gap of $Cu_{12-x}Zn_xSb_4S_{13}$ films varied from 1.49 to 1.6 eV, while the band gap of $Cu_{12}Sb_{4-x}Bi_xS_{13}$ films increased from 1.49 to 1.72 eV with increasing x. The effect of doping into the tetrahedrite on the lattice parameter and band gap energy was more significant in Bi-doped samples compared to Zn-doped samples. Optical measurements of the films suggest that $CuSbS_2$ and $Cu_{12}Sb_4S_{13}$ have direct band gaps of 1.44 and 1.49 eV respectively. This enables them to offer the most promising properties for use in solar energy conversion applications. The tuning of the magnitude of the band gap energy in these materials, and thus control over carrier concentration, is also interesting for thermoelectric applications. Overall, our approach represents a rapid, scalable, low temperature process toward these interesting materials.

Received: 18 September 2020; Accepted: 14 December 2020
Published online: 21 January 2021

References

1. Green Martin, A., Emery, K., Hishikawa, Y., Warta, W. & Dunlop Ewan, D. Solar cell efficiency tables (version 48). *Prog. Photovolt.* **24**, 905–913. https://doi.org/10.1002/pip.2788 (2016).
2. Jackson, P., Hariskos, D., Wuerz, R., Wischmann, W. & Powalla, M. Compositional investigation of potassium doped Cu(In, Ga) Se_2 solar cells with efficiencies up to 208%. *Phys. Status Solidi-R* **8**, 219–222. https://doi.org/10.1002/pssr.201409040. (2014).
3. Ansari, M. Z. & Khare, N. Effect of intrinsic strain on the optical band gap of single phase nanostructured Cu_2ZnSnS_4. *Mater. Sci. Semicond. Process.* **63**, 220–226. https://doi.org/10.1016/j.mssp.2017.02.011 (2017).
4. Thiruvenkadam, S., Jovina, D. & Leo Rajesh, A. The influence of deposition temperature in the photovoltaic properties of spray deposited CZTS thin films. *Sol. Energy* **106**, 166–170. https://doi.org/10.1016/j.solener.2014.02.041 (2014).
5. Wan, L. *et al.* Two-stage co-evaporated $CuSbS_2$ thin films for solar cells. *J. Alloys Compd.* **680**, 182–190. https://doi.org/10.1016/j.jallcom.2016.04.193 (2016).
6. Ramasamy, K., Sims, H., Butler, W. H. & Gupta, A. Selective nanocrystal synthesis and calculated electronic structure of all four phases of copper–antimony–sulfide. *Chem. Mater.* **26**, 2891–2899 (2014).
7. Yu, L., Kokenyesi Robert, S., Keszler Douglas, A. & Zunger, A. Inverse design of high absorption thin-film photovoltaic materials. *Adv. Energy Mater.* **3**, 43–48. https://doi.org/10.1002/aenm.201200538 (2012).
8. Tablero, C. Electronic and optical property analysis of the Cu–Sb–S tetrahedrites for high-efficiency absorption devices. *J. Phys. Chem. C* **118**, 15122–15127. https://doi.org/10.1021/jp502045w (2014).
9. Yang, B. *et al.* $CuSbS_2$ as a promising earth-abundant photovoltaic absorber material: A combined theoretical and experimental study. *Chem. Mater.* **26**, 3135–3143. https://doi.org/10.1021/cm500516v (2014).
10. van Embden, J. & Tachibana, Y. Synthesis and characterisation of famatinite copper antimony sulfide nanocrystals. *J. Mater. Chem.* **22**, 11466–11469. https://doi.org/10.1039/C2JM32094K (2012).
11. Yan, C. *et al.* Solution-based synthesis of chalcostibite ($CuSbS_2$) nanobricks for solar energy conversion. *RSC Adv.* **2**, 10481–10484. https://doi.org/10.1039/C2RA21554C (2012).
12. Qiu, X., Ji, S., Chen, C., Liu, G. & Ye, C. Synthesis, characterization, and surface-enhanced Raman scattering of near infrared absorbing Cu_3SbS_3 nanocrystals. *CrystEngComm* **15**, 10431–10434. https://doi.org/10.1039/C3CE41861H (2013).

13. Xu, D., Shen, S., Zhang, Y., Gu, H. & Wang, Q. Selective synthesis of ternary copper–antimony sulfide nanocrystals. *Inorg. Chem.* **52**, 12958–12962. https://doi.org/10.1021/ic401291a (2013).
14. Ikeda, S. *et al.* Selective production of $CuSbS_2$, Cu_3SbS_3, and Cu_3SbS_4 nanoparticles using a hot injection protocol. *RSC Adv.* **4**, 40969–40972. https://doi.org/10.1039/C4RA07648F (2014).
15. van Embden, J., Latham, K., Duffy, N. W. & Tachibana, Y. Near-infrared absorbing $Cu_{12}Sb_4S_{13}$ and Cu_3SbS_4 nanocrystals: Synthesis, characterization, and photoelectrochemistry. *J. Am. Chem. Soc.* **135**, 11562–11571. https://doi.org/10.1021/ja402702x (2013).
16. James, D. J., Lu, X., Morelli, D. T. & Brock, S. L. Solvothermal synthesis of tetrahedrite: Speeding up the process of thermoelectric material generation. *ACS Appl. Mater. Interfaces* **7**, 23623–23632. https://doi.org/10.1021/acsami.5b07141 (2015).
17. Manolache, S. A., Andronic, L., Duta, A. & Enesca, A. The influence of the deposition condition on crystal growth and on the band gap of $CuSbS_2$ thin film absorber used for solid state solar cells (SSSC). *J. Optoelectron. Adv. Mater.* **9**, 1269–1272 (2007).
18. Garza, C. *et al.* p-Type $CuSbS_2$ thin films by thermal diffusion of copper into Sb_2S_3. *Sol. Energy Mater. Sol. Cells* **95**, 2001–2005. https://doi.org/10.1016/j.solmat.2010.06.011 (2011).
19. Würfel, P. *Physics of Solar Cells* (Wiley, Weinheim, 2005).
20. Shockley, W. & Queisser, H. J. Detailed balance limit of efficiency of p-n junction solar cells. *J. Appl. Phys.* **32**, 510–519. https://doi.org/10.1063/1.1736034 (1961).
21. RodrÍGuez-Lazcano, Y., Nair, M. T. S. & Nair, P. K. CuxSbySz thin films produced by annealing chemically deposited Sb_2S_3-CuS thin films. *Mod. Phys. Lett. B* **15**, 667–670. https://doi.org/10.1142/S0217984901002257 (2001).
22. Rodríguez-Lazcano, Y., Nair, M. T. S. & Nair, P. K. $CuSbS_2$ thin film formed through annealing chemically deposited Sb2S3–CuS thin films. *J. Cryst. Growth* **223**, 399–406. https://doi.org/10.1016/S0022-0248(01)00672-8 (2001).
23. Suekuni, K. & Takabatake, T. Research update: Cu–S based synthetic minerals as efficient thermoelectric materials at medium temperatures. *APL Mater.* **4**, 104503. https://doi.org/10.1063/1.4955398 (2016).
24. Chetty, R., Bali, A. & Mallik, R. C. Tetrahedrites as thermoelectric materials: An overview. *J. Mater. Chem. C* **3**, 12364–12378. https://doi.org/10.1039/C5TC02537K (2015).
25. Heo, J. *et al.* Design meets nature: Tetrahedrite solar absorbers. *Adv. Energy Mater.* **5**, 1401506. https://doi.org/10.1002/aenm.201401506 (2014).
26. Lu, X., Morelli, D. T., Xia, Y. & Ozolins, V. Increasing the thermoelectric figure of merit of tetrahedrites by co-doping with nickel and zinc. *Chem. Mater.* **27**, 408–413. https://doi.org/10.1021/cm502570b (2015).
27. Heo, J., Laurita, G., Muir, S., Subramanian, M. A. & Keszler, D. A. Enhanced thermoelectric performance of synthetic tetrahedrites. *Chem. Mater.* **26**, 2047–2051. https://doi.org/10.1021/cm404026k (2014).
28. Loranca-Ramos, F. E., Diliegros-Godines, C. J., Silva González, R. & Pal, M. Structural, optical and electrical properties of copper antimony sulfide thin films grown by a citrate-assisted single chemical bath deposition. *Appl. Surf. Sci.* **427**, 1099–1106. https://doi.org/10.1016/j.apsusc.2017.08.027 (2018).
29. John, B., Genifer Silvena, G. & Leo Rajesh, A. Influence of reaction time on the structural, optical and electrical performance of copper antimony sulfide nanoparticles using solvothermal method. *Phys. B Condens. Matter* **537**, 243–250. https://doi.org/10.1016/j.physb.2018.02.030 (2018).
30. Suehiro, S. *et al.* Synthesis of copper–antimony–sulfide nanocrystals for solution-processed solar cells. *Inorg. Chem.* **54**, 7840–7845. https://doi.org/10.1021/acs.inorgchem.5b00858 (2015).
31. Wang, L. *et al.* Synthesis and characterization of hydrazine solution processed Cu12Sb4S13 film. *Sol. Energy Mater. Sol. Cells* **144**, 33–39. https://doi.org/10.1016/j.solmat.2015.08.016 (2016).
32. Chen, K. *et al.* Size-dependent synthesis of $Cu_{12}Sb_4S_{13}$ nanocrystals with bandgap tunability. *Part. Part. Syst. Char.* **32**, 999–1005. https://doi.org/10.1002/ppsc.201500088 (2015).
33. An, C., Jin, Y., Tang, K. & Qian, Y. Selective synthesis and characterization of famatinite nanofibers and tetrahedrite nanoflakes. *J. Mater. Chem.* **13**, 301–303. https://doi.org/10.1039/B210703A (2003).
34. Rath, T., MacLachlan, A. J., Brown, M. D. & Haque, S. A. Structural, optical and charge generation properties of chalcostibite and tetrahedrite copper antimony sulfide thin films prepared from metal xanthates. *J. Mater. Chem. A* **3**, 24155–24162 (2015).
35. Weller, D. P. *et al.* Thermoelectric performance of tetrahedrite synthesized by a modified polyol process. *Chem. Mater.* **29**, 1656–1664. https://doi.org/10.1021/acs.chemmater.6b04950 (2017).
36. Anderson, M. E., Bharadwaya, S. S. N. & Schaak, R. E. Modified polyol synthesis of bulk-scale nanostructured bismuth antimony telluride. *J. Mater. Chem.* **20**, 8362–8367. https://doi.org/10.1039/C0JM01424A (2010).
37. Barbier, T. *et al.* Thermoelectric materials: A new rapid synthesis process for nontoxic and high-performance tetrahedrite compounds. *J. Am. Ceram. Soc.* **99**, 51–56. https://doi.org/10.1111/jace.13838 (2015).
38. Lewis, E., Haigh, S. & O'Brien, P. The synthesis of metallic and semiconducting nanoparticles from reactive melts of precursors. *J. Mater. Chem. A* **2**, 570–580. https://doi.org/10.1039/C3TA12900D (2014).
39. Fischereder, A. *et al.* Solution-processed copper zinc tin sulfide thin films from metal xanthate precursors. *Monats. Chem.* **144**, 273–283. https://doi.org/10.1007/s00706-012-0882-6 (2013).
40. Kaltenhauser, V. *et al.* Bismuth sulphide-polymer nanocomposites from a highly soluble bismuth xanthate precursor. *J. Mater. Chem. C* **1**, 7825–7832. https://doi.org/10.1039/C3TC31684J (2013).
41. Alqahtani, T. *et al.* Synthesis of $Bi_{2-2x}Sb_{2x}S_3$ ($0 \leq x \leq 1$) solid solutions from solventless thermolysis of metal xanthate precursors. *J. Mater. Chem. C* **6**, 12652–12659 (2018).
42. Alqahtani, T., Cernik, R. J., O'Brien, P. & Lewis, D. J. Solid solutions of $M_{2-2x}In_{2x}S_3$ (M= Bi or Sb) by solventless thermolysis. *J. Mater. Chem. C* **7**, 5112–5121 (2019).
43. Sankir, N. D. & Sankir, M. *Printable Solar Cells* (Wiley, Hoboken, 2017).
44. Tang, Z. *Studies of Inverted Organic Solar Cells Fabricated by Doctor Blading Technique* Independent thesis Advanced level (degree of Master (Two Years)) thesis (2010).
45. Polfer, P., Fu, Z., Breinlinger, T., Roosen, A. & Kraft, T. Influence of the doctor blade shape on tape casting—Comparison Between analytical, numerical, and experimental results. *J. Am. Ceram. Soc.* **99**, 3233–3240. https://doi.org/10.1111/jace.14343 (2016).
46. Berni, A., Mennig, M. & Schmidt, H. Doctor blade. In *Sol-Gel Technologies for Glass Producers and Users* (eds Aegerter, M. A. & Mennig, M.) 89–92 (Springer, Boston, 2004).
47. Sivagami, A. D., Biswas, K. & Sarma, A. Orthorhombic $CuSbS_2$ nanobricks: Synthesis and its photo responsive behaviour. *Mater. Sci. Semicond. Process.* **87**, 69–76. https://doi.org/10.1016/j.mssp.2018.06.023 (2018).
48. Zhang, Z., Fu, Y., Zhou, C. & Lai, Y. Facile synthesis of $CuSbS_2$ blocks, and their lithium ion storage performance. *J. Electron. Mater.* **44**, 252–257. https://doi.org/10.1007/s11664-014-3499-1 (2015).
49. Shu, B. & Han, Q. Studies on structural, optical and electrical properties of $CuSbS_2$ nanoparticles. *Chalcogenide Lett.* **13**, 46–53 (2016).
50. Lu, X. *et al.* High performance thermoelectricity in earth-abundant compounds based on natural mineral tetrahedrites. *Adv. Energy Mater.* **3**, 342–348. https://doi.org/10.1002/aenm.201200650 (2012).
51. Barbier, T. *et al.* Structural stability of the synthetic thermoelectric ternary and nickel-substituted tetrahedrite phases. *J. Alloys Compd.* **634**, 253–262. https://doi.org/10.1016/j.jallcom.2015.02.045 (2015).
52. Chetty, R. *et al.* Thermoelectric properties of a Mn substituted synthetic tetrahedrite. *Phys. Chem. Chem. Phys.* **17**, 1716–1727. https://doi.org/10.1039/C4CP04039B (2015).

53. Chetty, R. *et al.* Thermoelectric properties of Co substituted synthetic tetrahedrite. *Acta Mater.* **100**, 266–274. https://doi.org/10.1016/j.actamat.2015.08.040 (2015).
54. Wang, J., Gu, M., Bao, Y., Li, X. & Chen, L. Quick fabrication and thermoelectric properties of Cu12Sb4S13 tetrahedrite. *J. Electron. Mater.* **45**, 2274–2277. https://doi.org/10.1007/s11664-015-4301-8 (2016).
55. Prem Kumar, D. S. *et al.* Thermoelectric properties of Cd doped tetrahedrite: $Cu_{12-x}Cd_xSb_4S_{13}$. *Intermetallics* **78**, 21–29. https://doi.org/10.1016/j.intermet.2016.08.003 (2016).
56. Koichiro, S., Kojiro, T., Tomoki, A. & Mikio, K. Thermoelectric properties of mineral tetrahedrites $Cu_{10}Tr_2Sb_4S_{13}$ with low thermal conductivity. *Appl. Phys. Express* **5**, 051201 (2012).
57. Nasonova, D. I. *et al.* Role of iron in synthetic tetrahedrites revisited. *J. Solid State Chem.* **242**, 62–69. https://doi.org/10.1016/j.jssc.2016.03.009 (2016).
58. Gonçalves, A. P. *et al.* Fast and scalable preparation of tetrahedrite for thermoelectrics via glass crystallization. *J. Alloys Compd.* **664**, 209–217. https://doi.org/10.1016/j.jallcom.2015.12.213 (2016).
59. Nasonova, D. I., Verchenko, V. Y., Tsirlin, A. A. & Shevelkov, A. V. Low-temperature structure and thermoelectric properties of pristine synthetic tetrahedrite $Cu_{12}Sb_4S_{13}$. *Chem. Mater.* **28**, 6621–6627. https://doi.org/10.1021/acs.chemmater.6b02720 (2016).
60. Harish, S., Sivaprahasam, D., Battabyal, M. & Gopalan, R. Phase stability and thermoelectric properties of $Cu_{10.5}Zn_{1.5}Sb_4S_{13}$ tetrahedrite. *J. Alloys Compd.* **667**, 323–328 (2016).
61. Nakada, T. *et al.* Gram-scale synthesis of tetrahedrite nanoparticles and their thermoelectric properties. *Langmuir* **35**, 16335–16340 (2019).
62. Tamilselvan, M. & Bhattacharyya, A. J. Tetrahedrite ($Cu_{12}Sb_4S_{13}$) ternary inorganic hole conductor for ambient processed stable Perovskite solar cells. *ACS Appl. Energy Mater.* **1**, 4227–4234. https://doi.org/10.1021/acsaem.8b00844 (2018).
63. Prem Kumar, D. S., Ren, M., Osipowicz, T., Mallik, R. C. & Malar, P. Tetrahedrite ($Cu_{12}Sb_4S_{13}$) thin films for photovoltaic and thermoelectric applications. *Sol. Energy* **174**, 422–430. https://doi.org/10.1016/j.solener.2018.08.080 (2018).
64. Hurma, T. & Kose, S. XRD Raman analysis and optical properties of CuS nanostructured film. *Optik* **127**, 6000–6006. https://doi.org/10.1016/j.ijleo.2016.04.019 (2016).
65. Chen, K. *et al.* Growth kinetics and mechanisms of multinary copper-based metal sulfide nanocrystals. *Nanoscale* **9**, 12470–12478. https://doi.org/10.1039/C7NR03576D (2017).
66. Buzatu, A. *et al.* Structural key features of bismuth and Sb-As sulfosalts from hydrothermal deposits—Micro-Raman spectrometry. *Vib. Spectrosc.* **89**, 49–56. https://doi.org/10.1016/j.vibspec.2017.01.002 (2017).
67. Johnson, N., Craig, J. & Rimstidt, J. D. Crystal chemistry of tetrahedrite. *Am. Mineral.* **73**, 389–397 (1988).
68. Pattrick, R. A. & Hall, A. Silver substitution into synthetic zinc, cadmium, and iron tetrahedrites. *Mineral. Mag.* **47**, 441–451 (1983).
69. Suekuni, K., Tomizawa, Y., Ozaki, T. & Koyano, M. Systematic study of electronic and magnetic properties for Cu12–xTMxSb4S13 (TM = Mn, Fe Co, Ni, and Zn) tetrahedrite. *J. Appl. Phys.* **115**, 143702. https://doi.org/10.1063/1.4871265 (2014).
70. Friese, K., Grzechnik, A., Makovicky, E., Balić-Žunić, T. & Karup-Møller, S. Crystal structures of iron bearing tetrahedrite and tennantite at 25 and 250 °C by means of Rietveld refinement of synchrotron data. *Phys. Chem. Miner.* **35**, 455–465. https://doi.org/10.1007/s00269-008-0240-8 (2008).
71. Shannon, R. D. Revised effective ionic radii and systematic studies of interatomic distances in halides and chalcogenides. *Acta Cryst.* **32**, 751–767. https://doi.org/10.1107/S0567739476001551 (1976).
72. Cullity, B. D. & Stock, S. R. *Elements of X-ray Diffraction* (Pearson Education, London, 2014).
73. May, A. F. *et al.* Structural phase transition and phonon instability in $Cu_{12}Sb_4S_{13}$. *Phys. Rev. B* **93**, 064104. https://doi.org/10.1103/PhysRevB.93.064104 (2016).
74. Battiston, S. *et al.* One step synthesis and sintering of Ni and Zn substituted tetrahedrite as thermoelectric material. *J. Alloys Compd.* **702**, 75–83. https://doi.org/10.1016/j.jallcom.2017.01.187 (2017).
75. Bera, S., Dutta, A., Mutyala, S., Ghosh, D. & Pradhan, N. Predominated thermodynamically controlled reactions for suppressing cross nucleations in formation of multinary substituted tetrahedrite nanocrystals. *J. Phys. Chem. Lett.* **9**, 1907–1912. https://doi.org/10.1021/acs.jpclett.8b00680 (2018).
76. Sarswat, P. K. & Free, M. L. Enhanced photoelectrochemical response from copper antimony zinc sulfide thin films on transparent conducting electrode. *Int. J. Photoenergy* **2013**, 7. https://doi.org/10.1155/2013/154694 (2013).
77. Prem Kumar, D. S. *et al.* Thermoelectric properties of Bi doped tetrahedrite. *J. Electron. Mater.* **46**, 2616–2622. https://doi.org/10.1007/s11664-016-4826-5 (2017).
78. Alqahtani, T. *et al.* Synthesis of $Bi_{2-2x}Sb_{2x}S_3$ ($0 \le x \le 1$) solid solutions from solventless thermolysis of metal xanthate precursors. *J. Mater. Chem. C* **6**, 12652–12659. https://doi.org/10.1039/C8TC02374C (2018).
79. Kharbish, S., Libowitzky, E. & Beran, A. Raman spectra of isolated and interconnected pyramidal XS_3 groups (X = Sb, Bi) in stibnite, bismuthinite, kermesite, stephanite and bournonite. *Eur. J. Miner.* **21**, 325–333. https://doi.org/10.1127/0935-1221/2009/0021-1914 (2009).
80. Mernagh, T. P. & Trudu, A. G. A laser Raman microprobe study of some geologically important sulphide minerals. *Chem. Geol.* **103**, 113–127. https://doi.org/10.1016/0009-2541(93)90295-T (1993).
81. Rabhi, A., Kanzari, M. & Rezig, B. Growth and vacuum post-annealing effect on the properties of the new absorber $CuSbS_2$ thin films. *Mater. Lett.* **62**, 3576–3578. https://doi.org/10.1016/j.matlet.2008.04.003 (2008).
82. Mak, K. F., Lee, C., Hone, J., Shan, J. & Heinz, T. F. Atomically thin MoS_2: A new direct-gap semiconductor. *Phys. Rev. Lett.* **105**, 136805 (2010).
83. Bincy, J., Genifer-Silvena, G. & Leo-Rajesh, A. Temperature dependent solvothermal synthesis of Cu–Sb–S nanoparticles with tunable structural and optical properties. *Mater. Res. Bull.* **95**, 267–276. https://doi.org/10.1016/j.materresbull.2017.07.026 (2017).

Acknowledgements

TA thanks the Imam Abdulrahman Bin Faisal University for the funding support and for allowing a period of study in the U.K., and also, the Saudi Arabian Cultural Bureau in London for their assistance and support. DJL and TA thank the EPSRC Core Capability in Chemistry EP/K039547/1 for providing some of the instrumentation used for characterisation, DJL also acknowledges funding from EPSRC standard grant EP/R022518/1 (Soft Processing to Enable the Low Impact, Sustainable Manufacture of Inorganic Materials and Advanced Inorganic Semiconductor Composites). MDK and DJL thank Africa Capacity Building Initiative program (Royal society-DFID) for financial support.

Author contributions

T.A.: performed experimental work, characterized materials, drafted the manuscript. M.D.K.: Conceptualized study, supervised first author in lab and helped to write the paper. D.J.L.: Principal investigator, conceptualized study, wrote and edited paper. X.L.Z.: Assisted with materials characterization by electron microscopy. P.O.B.: Provided useful suggestions and guidance.

Competing interests
The authors declare no competing interests.

Additional information
Supplementary Information The online version contains supplementary material available at https://doi.org/10.1038/s41598-020-80951-5.

Correspondence and requests for materials should be addressed to M.D.K. or D.J.L.

Reprints and permissions information is available at www.nature.com/reprints.

Publisher's note Springer Nature remains neutral with regard to jurisdictional claims in published maps and institutional affiliations.